Geology of the Snap Lake kimberlite intrusion, NW Territories, Canada: Field observations and their interpretation

T. M. Gernon[1], M. Field[2] & R.S.J. Sparks[3]

[1] School of Ocean and Earth Science, University of Southampton, Southampton, SO14 3ZH, UK

[2] DiaKim Consulting Limited, Wells Road, Wookey Hole, Wells, Somerset, BA5 1DN, UK

[3] Department of Earth Sciences, University of Bristol, Bristol, BS8 1RJ, UK

Running title: *Geology of the Snap Lake kimberlite intrusion*

ABSTRACT

The Cambrian (523 Ma) Snap Lake hypabyssal kimberlite intrusion, Northwest Territories, Canada, is a complex segmented diamond-bearing ore-body. Detailed geological investigations suggest that the kimberlite is a multi-phase intrusion with at least four different magmatic lithofacies. In particular, olivine-rich (ORK) and olivine-poor (OPK) varieties of hypabyssal kimberlite have been identified. Key observations are that the olivine-rich lithofacies has a strong tendency to be located where the intrusion is thickest and that there is a good correlation between intrusion thickness, olivine crystal size and crystal content. Heterogeneities in the lithofacies are attributed to variations in intrusion thickness and structural complexities. The geometry and distribution of lithofacies points to magmatic co-intrusion, and flow segregation driven by fundamental rheological differences between the two phases. We envisage that the low viscosity OPK magma acted as a lubricant for the highly viscous ORK magma. The presence of such low viscosity, crystal-poor magmas may explain how crystal-laden kimberlite magmas (> 60 vol.%)

are able to reach the surface during kimberlite eruptions. We also document the absence of crystal settling and the development of an unusual sub-vertical fabric of elongate olivine crystals, which are explained by rapid degassing-induced quench crystallisation of the magmas during and after intrusion.

KEY WORDS: kimberlite; magma; intrusion; Snap Lake; emplacement processes

---

This paper presents a field and petrographic description of an exceptionally well-exposed 2 to 3 m-thick hypabyssal kimberlite intrusion at Snap Lake Diamond Mine, NW Territories, Canada. We present data on intrusion thickness, lithofacies relationships, crystal size distributions, crystal fabric, crystal content and crystal concentration profiles. The Snap Lake intrusion provides important new insights into the architecture and emplacement processes of high-level magmatic plumbing systems.

Many processes can occur during magma transport or intrusion, including melting and solidification (Delaney & Pollard, 1982; Huppert & Sparks, 1988; Marsh, 1996), crystallisation and gravity-driven crystal fractionation (Shaw, 1965; Martin & Nokes, 1988; Blundy & Cashman, 2001, 2005), in-situ differentiation (Sparks et al., 1984; Mitchell, 2008), assimilation of wall-rock and contamination (Philpotts & Asher, 1993; Sparks et al., 2009), injection of different magma batches (Eichelberger, 1980; Eichelberger et al., 2000), magma mixing or unmixing (Sparks et al., 1977; McBirney, 1980; Spera, 2000; Couch et al., 2001), and flow differentiation (Komar, 1972a-b). Another key magmatic process is viscous segregation, which can occur during the co-intrusion of discrete magma batches (Carrigan, 2000). Where present in kimberlite intrusions, rheological segregation may have economic implications in that there could be variability in diamond size distributions within different magma batches. This provides an explanation for the juxtaposition of barren and economic hypabyssal kimberlite lithofacies. It is likely that a complex interplay of all these processes occurs during kimberlite ascent from the asthenospheric mantle to the upper crust.

Magma ascent rates are controlled by rheology and vary over several orders of magnitude. Ascent rates range from 0.001 to 0.15 m s^{-1} for basaltic magmas (Carrigan et al., 1992). Ar–Ar investigations of xenolith phlogopites (Kelley & Wartho, 2000), garnet dissolution studies (Canil & Fedortchouk, 1999) and dynamical and thermodynamic constraints (Sparks et al., 2006; Kavanagh and Sparks, 2009) suggest that kimberlite magmas are transported from the mantle to upper crustal levels in a matter of hours to days at velocities on the order of > 4 to 20 m s^{-1}. The timescales required for chemical corrosion and alteration observed in the host-rock adjacent to kimberlite intrusions requires stalling of magma at shallow to intermediate crustal levels prior to transport to the surface (Brown et al., 2007). Kimberlites are known to show evidence for in-situ differentiation (e.g., Dawson and Hawthorne, 1973), which is also indicative of magma stalling prior to eruption.

The intrusive emplacement of kimberlite magmas is usually considered a precursor to, or contemporaneous with diatreme–vent formation (Sparks et al., 2006; Mitchell, 2008). As such, detailed geological studies are needed to understand the dynamics of kimberlite eruptions. Snap Lake Mine presents excellent 3D exposures of a hypabyssal kimberlite intrusion. The kimberlite intrusion contains abundant large olivine crystals whose distribution and fabric provide constraints on rheological properties and emplacement processes. Its study constrains the large- and small-scale processes of kimberlite emplacement in the upper crust and may shed light more generally on the magmatic plumbing of diatreme–vent systems. The relationship between olivine abundance and grain size with diamond grade and distribution at Snap Lake is assessed elsewhere (Field et al., 2009).

GEOLOGICAL SETTING

The Snap Lake Diamond Mine is located ~220 km northeast of Yellowknife in the Northwest Territories of Arctic Canada (Fig. 1a). The Snap Lake Intrusion (SLI) is a complex segmented orebody comprising a series of sub-parallel sheets, dipping 5 to 30° towards the northeast. In parts of the mine, the SLI is exposed as a single well-defined intrusion, ranging in thickness between 0.1 and 15 m, but typically in the thickness range 3 to 5 m. In other areas there are multiple intrusions that are thought to be connected in three-dimensions. Multiple intrusions can extend over vertical distances of < 30 m in borehole intersections. A key and critical part of the intrusion are offsets or ‘steps’ and interconnections or ‘ramps’ between adjacent dyke segments, the location of which are commonly related to structural and compositional variability in the country rock.

The kimberlite was intruded in the Cambrian period (535 to 523 Ma; Agashev et al., 2001; Heaman et al., 2003, 2004) into complex deformed country rocks that form part of the Archaean Slave Province (Fig. 1b; Hammer et al., 2004). Country rocks in the Snap Lake area comprise granodiorites, tonalites and granites of the Defeat Pluton Suite (2610 to 2590 Ma) and metavolcanic rocks including layered amphibolites, high-grade metaturbidites and migmatites of the Yellowknife Supergroup (Figs. 1b to 1c; Stubley, 2000, unpublished data). The country rocks adjacent to the intrusion do not show any evidence of a thermal aureole. Underground the SLI crosses the NNW-SSE trending contact between the granitoids and metavolcanic rocks (Fig. 1e). The crustal stress regime likely governed the location and geometry of the intrusion, as has been reported at other kimberlite clusters (e.g. Venetia, South Africa; Kurszlaukis and Barnett, 2003). Although on a regional scale the intrusion is modelled as a continuous discordant sheet, locally it runs parallel to undulating foliations within the metavolcanic rocks, and a primary set of sub-horizontal joints within the granitoids (McBean et al., 2003). At Snap Lake, Archaean host rocks are cut by several northeast-trending Proterozoic faults (Fig. 1c) and by three suites of diabase dykes, of likely Paleoproterozoic age (LeCheminant and van Breemen, 1994; LeCheminant et al., 1997). The dextral strike-slip Snap Fault and associated structures (Fig. 1c) are related to the collision of the Slave and Churchill Cratons (1840 to 1735 Ma; Stubley, 2000). Although fault movement dominantly occurred >1.27 Ga (as constrained by Mackenzie diabase dykes), later reactivation occurred prior to kimberlite emplacement, resulting in normal high-angle displacements (Stubley, 2000). This process is thought to have produced extensive tension fracture systems dipping at low to intermediate angles to the north (M. McCallum, pers. comm.). The orientation of these fractures closely matches that of the SLI (Fig. 1d), and it is thought that these may have influenced kimberlite emplacement (Stubley, 2000).

OBJECTIVES & METHODOLOGY

Active workings at Snap Lake Mine (Figs. 1c & 1e) were mapped at 1 : 750 and 1 : 400 scales on mine-produced base maps. Mapping was undertaken in ramps (inclined tunnels used for haulage) and test panels (block excavations supported by multiple ore columns), both of which provided superb three-dimensional exposures. Here, mining ramps are referred to as tunnels to avoid confusion with the ramps or steps related to dyke emplacement. The intrusion is exposed in the main tunnels of the mine (zone 1, Fig. 1e) and test panels to the southeast (zone 2, Fig. 1e). Most of the outcrops described are exposed from 280 to 300 m elevation (Fig. 1d). For poorly accessible regions of the intrusion, geological information was gained from logging drill-core and drill-core records. The Snap Lake area has been intersected by 460 boreholes over a 12-year period, accounting for > 2.7 km of core. In general, the drill holes were evenly distributed across the area to facilitate early stages of exploration.

The architecture, structure and lithofacies of the intrusion were documented, and variations in texture, crystal (olivine) size distribution and crystal content in the intrusion were measured. Olivine crystal sizes were measured in a 1 m^2 grid using digital callipers at regularly spaced intervals, and measurements included maximum olivine size and the mean of the 5 largest olivine crystals. Crystal content (area %) was measured using a combination of visual estimates and image analysis employing high-resolution oriented photographs of rock faces. Sub-vertical graphic logs and crystal concentration profiles were constructed through sections of the intrusion at regular intervals (perpendicular to the margins). Image analysis was used to quantify olivine crystal fabrics. Images of olivine crystals were digitised in the image analysis program, ImageJ (NIH, 2006), which provided major axis measurements, together with the angles of these major axes from the horizontal. These data were then plotted in the "R" program (R, 2006) that generated rose diagrams depicting crystal axis orientation and length. Polished slabs and thin sections were produced from representative samples of each lithofacies in the intrusion. Petrography was carried out using an optical microscope and a HITACHI S-3500 N Scanning Electron Microscope. Ogilvie-Harris et al. (2009) present a detailed study of the petrology of the intrusion.

TERMINOLOGY

We adopt the definition of a *hypabyssal kimberlite* as "a hybrid rock consisting of mantle-derived xenocrysts and primary phases that crystallised from the magma" (Mitchell, 1986, 2008). The term *macrocryst* is used to describe anhedral-to-subhedral crystals, which are typically > 0.5 mm in diameter and inferred to be mantle-derived. In the following description, we distinguish *macrocrysts* using the terms *fine*, *medium*, *coarse* and *very coarse* to describe grains with the following respective diameters: 0.5 – 2 mm, 2 – 6 mm, 6 – 20 mm and > 20 mm. The term *microcryst* refers to small (< 0.5 mm diameter) groundmass crystals. We use the term *olivine* to refer to a *serpentinised olivine pseudomorph*. In discussing crystal orientations, the term *sub-vertical fabric* is used to describe the dominant inclination of elongate macrocrysts within 10° of the vertical with respect to the intrusion contacts. A *sub-horizontal fabric* refers to the imbrication of elongate crystals within 10° of the horizontal relative to the intrusion contacts. The term *ramp* is used to describe thin (typically 0.1 – 1 m diameter), relatively high angle (10º – 40º) dilations within the intrusion, which cut through the country rock connecting adjacent intrusion segments. In this paper, we follow the terminology introduced to kimberlite geology by Sparks et al. (2006).

FIELD AND PETROGRAPHIC OBSERVATIONS

The SLI is typically a moderate to highly porphyritic hypabyssal intrusion consisting of suspended altered olivine crystals in a fine-grained matrix (Fig. 2a). The rock is pervasively altered; fresh olivine has not yet been found and all olivine crystals are pseudomorphed by serpentine. Calcite and dolomite are present, both in the interstices between crystals and as lenticular veins, which commonly cut across original igneous textures and fabrics. Alteration varies in style; for example, olivine is commonly replaced by pale (low Mg) serpentine and in some zones by dark (high Mg) serpentine. The proportion of olivine crystals varies significantly throughout the intrusion. In places, the content of macrocrysts is ≥ 20% and here it is defined as olivine-rich. Where the crystal content is < 20%, it is defined as olivine-poor. This threshold was chosen because samples show bimodality in crystal content and 20% is approximately the boundary between the two groups.

Kopylova et al. (2010) describe the mineralogy of Snap Lake kimberlites, and interpret the OPK to represent a pervasively altered version of ORK. However, the alteration model presented in Kopylova et al. (2010) is inconsistent with our field observations and petrological investigations. Below, we present detailed textural observations and measurements of the kimberlites, which provide compelling evidence for a discrete olivine-poor kimberlite (OPK) lithofacies. Further support for the existence of OPK and ORK is given by the contrasted mineralogical and petrological characteristics of the two key lithofacies (Ogilvie-Harris et al., 2009). Additional evidence for a complex multi-phase emplacement is provided by anisotropy of magnetic susceptibility (AMS) analyses, which demonstrates at least two distinct flow directions attributed to a late-stage second phase of kimberlite magma within the intrusion (O'Keefe and Cruden, 1999).

Textural variations

Olivine-rich hypabyssal kimberlite (ORK)

The olivine-rich lithofacies typically has a massive appearance (Figs. 2a), and dominantly comprises fine to coarse olivine macrocrysts (20 to 75 area %; Figs. 2a-b), olivine microcrysts (10 to 50 area %; Fig. 2c-d), very coarse macrocrysts (~5 area %), and a range of country rock xenoliths (typically 2 to 10 area %, locally ≥ 25 area %). The country-rock xenoliths are restricted in distribution, and tend to occur near major offsets in the segmented intrusion. In thin section, serpentine both replaces olivine and is recognised in the interstices between crystals.

Some pseudomorphed groundmass microcrysts may be after monticellite rather than olivine based on their equant shapes (e.g. Fig. 2d). Complex intergrowths of serpentine and apatite are observed. Secondary dolomite occurs in the interstices between crystals. Together with serpentinised olivine, groundmass components include phlogopite (3 to 20%), apatite (3 to 10%), chrome spinel (~ 1%), rutile (~ 1%) and titanite (< 1%). Phlogopite and apatite are typically highly localised and occur in small (100 to 500 μm diameter) accumulations. In general, the ORK contains relatively large (0.1 to 1 mm) elongate phlogopite laths, commonly exhibiting decussate textures.

Olivine crystal fabrics: Olivine macrocrysts are generally anhedral-to-subhedral and typically elongate, with length : width ratios ranging between 2 : 1 to 10 : 1. At an outcrop scale, a preferred sub-vertical alignment fabric of olivine long axes (i.e. perpendicular to the intrusion walls) is commonly seen (Fig. 2a-c). The fabric orientation is generally consistent over lateral distances of tens of metres (Fig. 3), but typically varies vertically in the intrusion (e.g. Fig. 3, logs 2 & 3). Within olivine-rich regions, the crystal content occasionally increases in cm-dm scale patches so that the crystals are densely packed (60 to 75 area %).

Figure 3 shows a graphic log through a typical section of hypabyssal kimberlite from zone 1 of the intrusion (Fig. 1e). The crystal content is uniform throughout, with the exception of relatively thin (0.3 – 1 m) regions of olivine-poor kimberlite (OPK, described below) at the top and bottom of the intrusion. Several traverses show an increase in crystal size towards the centre of the intrusion (e.g. Fig. 3, logs 4 & 6). Crystal orientations are generally random in the upper 0.5 metres (e.g. Fig. 3, log 2). The central crystal-rich zone exhibits steeply inclined fabrics, ranging from 60° to 90° relative to the intrusion margins (Fig. 3). The basal metre also shows strong fabrics, with macrocrysts being inclined at 50º to 80º (from W to E, e.g. Fig. 3, log 2). A similar fabric is developed near the base of the ORK component of profile ND1-01 (see Fig. 1e), where macrocrysts are strongly inclined at angles ranging from 10° to 75° (from SW to NE; Fig. 4). However, in this part of the intrusion, macrocryst orientations are generally highly variable (Fig. 4).

Olivine-poor hypabyssal kimberlite (OPK)

The olivine-poor kimberlite (OPK) lithofacies is characterised by a relatively low proportion of fine to medium olivine macrocrysts (5 to 20 area %; Figs. 5a-b), a paucity of coarse olivine macrocrysts and mantle nodules (< 5 area %), and a high abundance of phlogopite crystals (typically 30 to 60 area %). Phlogopite is particularly abundant immediately adjacent to the country rock contact. In most cases, the distribution of crystals is heterogeneous, giving the rock a very patchy appearance (Fig. 5b).

Olivine crystal orientations are typically random in the OPK (e.g. Fig. 4, section (a)), but occasionally sub-horizontal relative to the boundaries of the intrusion (e.g. Fig. 3, log 4). In the OPK, olivines occur mainly as small microcrysts, commonly separated by elongate phlogopite laths (Figs. 5c–d). The olivine grain boundaries are poorly discernible, constituting amorphous masses of serpentine. Phlogopite (Ti-rich and Ti-poor varieties) generally occurs as relatively large laths (100 to 750 μm) in the OPK. The phlogopite laths commonly contain inclusions of chromite, Ti-rich spinel (with atoll textures), rutile, and small serpentinised equigranular crystals; the latter are thought to be pseudomorphs after monticellite. Phlogopite crystals commonly exhibit random orientations (Figs. 5c–d), though towards the upper and lower contacts are strongly aligned parallel to the intrusion contact. The interstitial groundmass contains secondary serpentines (Mg-rich and Mg-poor) and dolomite.

Rare apatite in the OPK lithofacies typically occurs as small isolated grains (~20 μm; Fig. 5c) in contrast to the ORK lithofacies (Figs. 2c–d). Some domains of the crystal-poor lithofacies, particularly towards the intrusion margins, contain pervasive veins in which olivine is replaced by vermiform serpentine (antigorite), and an interstitial cement of serpentine, dolomite and altered phlogopite (Fig. 5e). Phlogopite is pervasive throughout the intrusion, with the exception of a 0.5 m thick olivine-rich section in the upper-central part, where the small phlogopite (< 200 μm diameter) is less common (see Journal of the Geological Society website, supplementary figure S1). In profile ND2-06 (Fig. 1e), a third textural variant occurs in the lower third of the intrusion and contains both abundant serpentinized olivine macrocrysts as well as phlogopite phenocrysts (Fig. S1).

Kopylova et al. (2010) interpret the OPK lithofacies as highly altered ORK; however psuedomorphs of large olivine crystals were not observed, and a high proportion of the rock is composed of a fine-grained phlogopite-rich groundmass (Fig. 5). Kopylova et al. (2010) suggest that the pholOgopite may be derived from contamination of the melt by granite xenoliths, however no evidence for this is provided and it remains unclear how this process could occur to such an extent in a thin rapidly emplaced and cooled intrusion.

Intrusion thickness, crystal size and crystal content

Wide variations in maximum olivine crystal size are observed across the intrusion (see Fig. 6 and Journal of the Geological Society website, supplementary figure S2). There is a very good relationship between intrusion thickness and maximum crystal size (Fig. 6a). Below an intrusion thickness of approximately 3 m, there is a positive correlation between intrusion thickness and maximum crystal size (Fig. 6a), however above this thickness, the crystal size increases significantly (Fig. 6a). Olivine crystal content (area %) also increases with intrusion thickness and is positively correlated up to a thickness of 2.8 to 3 metres, at which point a significant increase in crystal content occurs (Figs. S2 & 6b). These relationships are supported by observations from drill-core, where occurrences of olivine-poor kimberlite are generally confined to intrusion thickness ≤ 1.5 m; approximately 65% of all intrusion intervals recorded below this threshold range in thickness between 0.05 to 0.3 m.

Field relations

In the southeastern part of the mine (zone 2, Fig. 1e), the SLI is approximately 3 to 4 m thick and the internal stratigraphy of the intrusion varies over metre- to tens of metre-scales. Zone 2 comprises multiple NW-SE orientated ramps, which generally dip toward the NE with displacement magnitudes ranging from 0.6 to 2.6 metres (Fig. 7a). Here, hypabyssal kimberlite typically comprises densely packed, coarse to very coarse macrocrystic olivines and mantle xenoliths (e.g. Fig. 2a). The maximum olivine crystal size varies laterally; most of the area is dominated by very coarse crystals, whereas to the south a domain of smaller crystals is identified (Fig. 7b). The mean of the five largest crystals show less lateral variability (Fig. 7c). Crystal proportions tend to vary significantly over short distances (Fig. 7d). For example, one ramp structure involves a change in crystal content from 25 area % to 50 area % over a lateral distance of 5 to 10 metres (Figs. 7b and 8). Crystal content also varies vertically within the intrusion (see Journal of the Geological Society website, supplementary figures S3 – S5). Key observations from these sections are that the centre of the intrusion is olivine-rich and that the margins are olivine-poor, although inversion of the OPK–ORK stratigraphy occurs over tens of metre scales (see Fig. S3).

Laterally extensive ORK lenses

Thick lenses of ORK (~0.5 to 2 m) occur prominently in the OPK (Fig. 8), and thin out over distances of 5 to 20 m. The lenses are reminiscent in geometry and stratigraphic position to phenocryst-rich tongues recorded in the Basement Sill of the Ferrar dolerite sill complex (Charrier & Marsh, 2004; Petford et al., 2005; Bédard et al., 2007), albeit on a smaller scale. Commonly, these lenses branch out laterally into several lobes (Fig. S4), which wedge out in thinner intrusion segments, typically across structural obstacles such as ramps (Fig. 8).

Cognate xenoliths

Cognate xenoliths occur in the SLI, and tend to cluster in the upper metre of the intrusion within the OPK lithofacies. They also occur in the ORK lithofacies, where they form sharp boundaries with the ORK. Commonly the xenoliths are sub-circular to elongate, pod-like, and range in diameter from 15 to 150 cm. In the OPK, they are medium to very coarse grained (average crystal diameter = 5 mm) and olivine rich. Occasionally, they exhibit diffuse boundaries with the OPK, with large olivine macrocrysts and fragments of the cognate xenoliths in the surrounding OPK matrix. Crystals within the xenoliths show strong preferred alignments, typically sub-parallel to the intrusion walls. Regions of fine-grained phlogopite-rich, OPK (cm to dm scale) occur in the ORK, where they are characterised by contorted boundaries and patchy crystal size distributions.

Lithic breccia lithofacies

Locally, the SLI contains lithic breccia lithofacies comprising coarse to very coarse (typically ≤ 1 cm diameter) olivine macrocrysts, which are highly concentrated (~50 vol.%) and densely packed in the interstices between locally derived angular lithic clasts (Fig. 9a). The breccias are highly weathered and consequently difficult to sample. The coarse olivine macrocrysts occur within pods in sharp contact with the OPK (Fig. 9a). Such breccia zones are unconfined and laterally continuous over tens of metres (Fig. 1e). A second breccia lithofacies is olivine-poor (5 area %) to moderately (15 area %) rich (Fig. 9b). This type of breccia is typically a localised, wedge-shaped feature (Fig. 9b), occurring in the hangingwall of the intrusion associated with ramp systems. Both lithofacies are matrix-supported with subordinate patches of clast-supported breccia developed locally, particularly adjacent to ramp structures. The breccia lithofacies account for approximately 5 to 8 vol.% of the intrusion.

In the vicinity of ramps, the intrusion is characteristically disrupted and enriched in shattered country rocks (Fig. 9c). Commonly, lozenge-shaped regions enriched in xenoliths (25 to 40 vol.%) are confined to the centre of the intrusion, though isolated slab-like fragments occur in the uppermost 0.5 metres where they rest on the ORK-OPK contact. In many cases, the proportion of xenoliths decreases along the intrusion away from ramp structures (Fig. 9c) over lateral distances on the order of 20 metres (Fig. 9d). Intrusion thickness is highly variable in ramp zones, probably due to the irregular structure of the metavolcanic host-rock. All these data demonstrate that significant variations in lithofacies geometry and crystal size, crystal content, crystal distribution and xenolith content occur over short distances (metres to tens of metres) in the Snap Lake intrusion.

DISCUSSION

The Snap Lake kimberlite is a discordant thin intrusion composed of various hypabyssal lithofacies. The two end-member lithofacies are petrologically and geochemically distinct (Ogilvie-Harris et al., 2009). Together, textural, mineralogical and geochemical differences point towards the two lithofacies representing different magmatic phases that have undergone different processes during ascent and emplacement. Magma batches with different characteristics have been observed in other kimberlite intrusions (e.g. Wesselton and Lethlakhane; Sparks et al., 2006, 2009).

Formation of the lithic breccia lithofacies

The structure and lithofacies of complex ramp zones in the SLI are consistent with a multi-stage formation. Firstly, magma is transported through propagating intrusion segments, and a radial fracture network develops around the tips of the intrusion splays (Fig. 10a). Both sets of fractures then interact, and a major fracture system develops between the intrusions (i.e. bridge zone), where the country rock is fragmented. Eventually, magma forces its way through the fractures, the intrusion segments connect and a ramp is formed (Fig. 10b). The original intrusion tips are preserved as dead splays (Figs. 9c & 10c). Finally, strong inflation and dilation occurs to accommodate increased magma flow (Fig. 10c). Fractures in the bridge of the ramp zone contribute shattered lithic material to the intrusion. Several features of the breccia lithofacies, such as localisation of coarse components and lateral continuity and geometry of the bodies, can be explained by explosive flow emplacement associated with inflation of the intrusion. Isolated slab-like blocks in the upper metre of the intrusion are attributed to stoping from the metasedimentary host rock.

Importance of magma viscosity

Crystal-laden magmas are known to exhibit complex rheological behaviour (Pinkerton & Stevenson, 1992; Spera, 2000; Castruccio et al., 2010). As such, the major textural differences between OPK and ORK lithofacies imply markedly different rheological properties during magma transport (Fig. 11). Relative to crystal-free magmas (i.e. melt), crystal-rich magmas can have much higher viscosities and can develop non-Newtonian rheologies (see Castruccio et al., 2010, and references therein).

The viscosity of kimberlite melts have been estimated to lie in the range 0.1 – 1 Pa s (Sparks et al., 2006). The fraction of suspended olivine crystals in the SLI typically varies between 0.05 and 0.6. To estimate the groundmass viscosity, μ_g (i.e. viscosity of a mixture of melt and very small crystals formed prior to or during emplacement, which subsequently form the groundmass), we apply a modified Einstein-Roscoe equation (Roscoe, 1952; Castruccio et al., 2010), over a range of melt viscosities (0.1, 1 and 100 Pa s). Castruccio et al. (2010) relates the melt and groundmass viscosity by the equation:

$$\mu_g = \mu_{melt}(1-\frac{\phi}{\phi_m})^{-2.3} \quad (1)$$

where μ_{melt} is the melt viscosity, ϕ is the crystal content, and ϕ_m is the maximum packing fraction. Figure 12a shows the variation of μ_g as a function of ϕ, taking $\phi_m = 0.65$. If we assume that the OPK melt has a low viscosity of 0.1 Pa s, and a representative crystal content of 10 vol.%, the magma viscosity will lie in the range 0.15 – 0.2 Pa s. When the crystal content reaches about 60%, large increases in yield strength (τ_y) and viscosity occur (Marsh, 1981; Philpotts and Carroll, 1996; Smith, 2000; Caricchi et al., 2007). Above some threshold crystal content, the magma behaves as a partially molten solid and equation 1 no longer applies (Costa, 2005). For example, an increase in crystal content from 0 to 0.6 will increase the groundmass viscosity from 0.1 to 365 Pa s. The texture and grain-size distribution of the ORK lithofacies suggests that it was emplaced as a partly solidified crystal mush (c.f. Charrier & Marsh, 2004; Petford et al., 2005;

Bédard et al., 2007) in a plug flow regime (Komar, 1972a; Ross, 1986; Ventura et al., 1996).

The complex spatial relationships observed between the OPK and ORK lithofacies (Figs. 10 & 12) can be explained by a two-component magma flow (c.f. Ross, 1986; Carrigan and Eichelberger, 1990). Field, experimental and theoretical studies of two-component flows have shown that it is common for low-viscosity components to flow in advance of high-viscosity components, lubricating their passage (Carrigan and Eichelberger, 1990; Koyaguchi and Takada, 1994; Carrigan, 2000). The high viscosity component is confined to a zone of weaker shear in the intrusion centre, and the pressure gradient required to drive the high viscosity component through the intrusion is substantially reduced (Komar, 1976; Barrière, 1976; Carrigan and Eichelberger, 1990; Carrigan, 2000). This process does not require the magmas to be genetically related, and can explain the observed lithofacies variations (Figs. 3 & 8) and lateral inversion of the OPK–ORK stratigraphy commonly observed in the SLI (Figs. S3 & 11a).

Absence of crystal settling and magma solidification

A key feature in the Snap Lake intrusion is the general absence of size grading (see Figs. 3 & S1). In addition, large (≤ 2 m) locally derived country rock xenoliths are commonly observed to rest upon the upper contact of the ORK lithofacies at the base of the OPK, suggesting that the ORK had crystallised extensively before solidification of the OPK. Here, we present calculations on the timescales of crystal settling, which are then compared with the timescale for conductive cooling of the intrusion. A magma density (ρ_f) of 2800 kg m^{-3} is assumed (Sparks et al., 2006) and the density of olivine (ρ_s) is taken as 3300 kg m^{-3} (i.e. $\Delta\rho$ = 500 kg m^{-3}). The terminal velocity of a crystal settling through the melt phase only (U_t) depends on the particle Reynolds number (Re_p) and is calculated by:

$$U_t = \frac{z}{t} = \frac{g(\rho_s - \rho_f).{d_p}^2}{18\mu_{melt}} \qquad (\mathrm{Re_p} < 0.4) \qquad (2)$$

$$U_t = \frac{z}{t} = \left(\frac{4.(\rho_s - \rho_f)^2.g^2}{225.\rho_g.\mu_{melt}}\right)^{\frac{1}{3}} d_p \qquad (0.4 < \mathrm{Re_p} < 500) \qquad (3)$$

where z is the intrusion thickness (assumed to be horizontal), t is the timescale for crystal settling and g is gravitational acceleration. Fig. 12b shows the settling timescale of a 1 cm olivine crystal as a function of distance and melt viscosity.

Terminal velocity is reduced due to hindered settling through regions of locally high crystal concentration. Richardson (1971) equates the average fall velocity of a crystal in a dispersion (U) by the relation:

$$U = U_t.E^n \quad (4)$$

where E is the voidage (or volume of melt in unit volume of dispersion). The power n is a function of Re_t in the melt phase only:

$$n = 4.65(\mathrm{Re}_t < 0.2) \quad (5)$$

$$n = 4.4\,\mathrm{Re}_t^{-0.03}(0.2 < \mathrm{Re}_t < 1) \quad (6)$$

$$n = 4.4\,\mathrm{Re}_t^{-0.1}(1 < \mathrm{Re}_t < 500) \quad (7)$$

For large olivine macrocrysts settling through a mixture of melt and suspended small groundmass crystals, we choose d_p = 0.01 m, and a range of crystal contents (ϕ = 0.3 – 0.5) in the intrusion (see Figs. 3, 6 & S2). Figure 12c shows the timescale for crystal settling as a function of depth in the intrusion using equation 6 for a melt viscosity of $\mu = 0.1$ Pa s. Hindered settling increases crystal settling times (Fig 12c), but these remain much less than the intrusion cooling time. To a first approximation, the Snap Lake intrusion would take 55 – 60 days to cool (Fig. 12c), given a representative dyke thickness of 4 m and thermal diffusivity of 8×10^{-7} m^2 s^{-1}. The timescale for crystal settling (Fig. 12b-c) is therefore substantially shorter (10^{2-4} times) than that of conductive cooling of the intrusion for all reasonable geological conditions. In order for settling times to equal cooling times, and assuming a very high crystal content (60%), the primary melt viscosity would have to be on the order of 10^3 - 10^4 Pa s. Although kimberlite melt compositions, temperatures and volatile contents are poorly constrained with much uncertainty (Sparks et al., 2009), the evidence from field relationships, pyroclast textures and experiments on silica-poor melts is that the viscosities are very low. Sparks et al. (2006) summarised the evidence and concluded that they are likely less than 1 Pa s.

Fabric development

Crystal preferred orientations within intrusions are typically developed parallel to the walls (i.e. parallel to the magma flow; Blanchard et al., 1979; Higgins, 2006), as documented in studies such as Shelley (1985), Ross (1986), Greenough et al. (1988), Wada (1992) and Philpotts & Asher (1994). Within the OPK, a sub-horizontal alignment fabric (Fig. 3) indicates intrusion-parallel flow. We propose that the sub-vertical alignment fabric in the ORK (Figs. 2 & 3) was generated during intrusion inflation (Fig. 11b). The elongate olivine crystals were initially aligned parallel to the magma flow and the intrusion walls, and were subsequently stretched into more stable sub-vertical orientations parallel to σ_3 during inflation (Fig. 11b). Shearing of crystals is occasionally observed near the base of the ORK lithofacies (e.g. Fig. 4f); this is attributed to a combination of pure shear related to mechanical compaction of the crystal mush (cf. Petford et al., 2005), and simple shear due to lateral flow of the OPK fluid. Random crystal orientations recorded towards the centre of the intrusion at several localities (e.g. Fig. 4) may support the presence of a plug region as documented in high-viscosity Bingham magmas (Ross, 1986) and lava flows (Ventura et al., 1996).

Cognate xenoliths

Cognate xenoliths are a common feature in magmatic intrusions (Green & Ringwood, 1967; Preston & Bell, 1997) and are typically found in the uppermost metre of the SLI within the OPK lithofacies (Fig. 8). The xenoliths are texturally and compositionally similar to the underlying ORK. We infer that the xenoliths were eroded from the ORK by the relatively mobile OPK magma and transported laterally along the intrusion margins (Fig. 11a). Diffuse boundaries to the xenoliths suggest that they were not fully solidified when this occurred. Together, these features demonstrate that the OPK magma post-dated at least part solidification of the ORK magma. The cognate xenoliths, branching lobes and interfingering of the OPK and ORK indicate that the two magmatic phases are broadly contemporaneous. The distinct textural and geochemical differences between the lithofacies (Ogilvie-Harris et al., 2009) can be explained by separate magma batches that sampled the mantle in varying efficiency and were emplaced contemporaneously. The OPK magma likely represents a more evolved liquid, which has lost most of its phenocrystal olivines, mantle components and spinel and undergone crystal-liquid differentiation during transit and stalling (Price et al., 2000). The occurrence of segregation processes en route to the surface is supported by significant differences in diamond size distributions between the ORK and OPK (Field et al., 2009). It is likely that kimberlite magmas ascending from depths of ~150 to 200 km will differentiate at choke points in branching vein and dyke systems, leading to crystal accumulation, slurry formation and melt segregation (Mitchell, 2008).

Intrusion heterogeneity explained by thickness variation and flow duration?

In larger intrusive complexes (e.g. the Basement Sill, Antarctica), the thickness of crystal-rich lithofacies is directly related to the location of feeder intrusions (Charrier & Marsh, 2004). Since the SLI represents an inclined sheet with no recognised feeder intrusions (Fig. 1d), the lithofacies distribution and architecture are attributed to intrusion thickness and flow duration. The observed relationships between intrusion thickness, crystal size and crystal content in the SLI (Fig. 6) strongly suggest a change in flow behaviour over a threshold thickness of ~2.8 metres. Further evidence is provided by the lensing out of ORK into thinner intrusion segments (e.g. Fig. 8). Field and fluid dynamical investigations of other sheet intrusions (e.g. sills) reveal that sustained flow is only possible in regions where the thickness exceeds 3 to 3.5 metres (Holness & Humphreys, 2003). Sustained flow may have occurred in thick (≥ 2.8 m) parts of the SLI, explaining the observed high concentrations of large crystals in thicker intrusion segments (see Figs. 6 – 7 & S2).

Degassing-induced crystallisation

There is a large discrepancy between crystal settling time, even at high crystal fractions (Fig. 12c), and cooling time (Fig. 12c) of the intrusion. Even accounting for hindered settling through a crystal mush, olivine crystals should have settled easily and very rapidly if the groundmass were a melt (Fig. 12b-c). The observed absence of size grading (see Fig. 3), and the preservation of a strong sub-vertical fabric (Figs. 2 – 3) can be explained by pervasive internal groundmass crystallisation during and after emplacement; this would lead to highly elevated magma viscosities and abrupt solidification (Sparks et al., 2006). It is proposed that fabric generation coincided with quench crystallisation of decussate phlogopite crystals, observed in the interstices between large crystals and attributed to rapid degassing during emplacement (c.f. Bacon, 1986).

CONCLUSIONS

Detailed geological mapping has demonstrated that the Snap Lake hypabyssal kimberlite intrusion is texturally heterogeneous, comprising olivine-rich and olivine-poor lithofacies. The lithofacies are petrologically distinct suggesting that the SLI is a multi-phase intrusion, emplaced by at least two magma batches. The variation in crystal content of the ORK and OPK indicates fundamental rheological differences between the magmas and different flow processes during transport and emplacement. The occurrence and nature of branching lobes, cognate xenoliths, internal stratigraphic zonation and lateral lithofacies variations can be explained by a combination of thickness variations and flow transformations due to the preferential flow of low-viscosity magma around high-viscosity magma, and associated localisation of shear along the walls. This “lubrication” process explains how highly viscous, crystal rich (> 60 vol.%) kimberlite magmas are transported to the surface to erupt in diatremes. The results show a moderate to strong correlation between intrusion thickness and crystal size and crystal content, which has important implications for diamond distributions in kimberlite intrusions. A marked change in crystal size and content occurs at a thickness of approximately 3 m, probably due to a change in flow regime at this level as documented in other sheet intrusions. In addition, significant changes in crystal size, content and concentration profiles occur laterally over metre to tens of metre scales in the intrusion. The observed lack of grading and preservation of a sub-vertical fabric within the Snap Lake intrusion suggests that groundmass crystallisation occurred rapidly during and after emplacement. The emplacement processes outlined in this paper are potentially important in other types of sub-volcanic sheet intrusions, particularly those associated with mafic and ultramafic diatreme–vent systems.

ACKNOWLEDGEMENTS

This work was funded by De Beers Canada with support from the De Beers MRM R&D Group, Wells. We acknowledge the input of Dr Malcolm Thurston (De Beers Canada) together with Josh Harvey and the staff of the geology department at Snap Lake Mine. Nicholas Arndt, Chris Bonson, Thea Hincks, Thierry Menand, Madeleine Humphreys, and Rachael Ogilvie-Harris are thanked for helpful discussions. We are grateful to Kelly Russell and Dante Canil for their thorough reviews.

REFERENCES

Bacon, C. R. (1986). Magmatic inclusions in silicic and intermediate volcanic rocks. *Journal of Geophysical Research* 91, 6091-6112.

Barrière, M. (1976). Flowage differentiation: Limitation of the “Bagnold effect” to the narrow intrusions. *Contributions to Mineralogy and Petrology* 55 (2), 139-145.

Bédard, J. H. J., Marsh, B. D., Hersum, T. G., Naslund, H. R. & Mukasa, S. B. (2007). Large-scale mechanical redistribution of orthopyroxene and plagioclase in the Basement Sill, Ferrar

Dolerites, McMurdo Dry Valleys, Antarctica: Petrological, mineral-chemical and field evidence for channelized movement of crystals and melt. *Journal of Petrology* 48 (12), 2289-2326.

Blanchard, J. P., Boyer, P., & Gagny, C. (1979). Un nouveau critère de sens de mise en place dans une caisse filonienne: le "pincement" des minèreaux aux èpontes. *Tectonophysics* 53, 1-25.

Blundy, J. D. & Cashman, K. (2001). Ascent-driven crystallisation of dacite magmas at Mount St Helens, 1980-1986. *Contributions to Mineralogy and Petrology* 140 (6), 631-650.

Blundy, J. D. & Cashman, K. (2005). Rapid decompression-driven crystallization recorded by melt inclusions from Mount St. Helens volcano. *Geology* 33 (10), 793-796.

Brown, R. J., Kavanagh, J., Sparks, R. S. J., Tait M. & Field, M. (2007). Mechanically disrupted and chemically weakened zones in segmented dyke systems cause vent localisation: evidence from kimberlite volcanic systems. *Geology* 35, 184-188.

Canil, D. & Fedortchouk, Y. (1999). Garnet dissolution and the emplacement of kimberlites. *Earth and Planetary Science Letters* 167, 227-237.

Caricchi, L., Burlini, L., Ulmer, P., Gerya, T., Vassalli, M. & Papale, P. (2007). Non-Newtonian rheology of crystal-bearing magmas and implications for magma ascent dynamics. *Earth and Planetary Science Letters* 264 (3-4), 402–419.

Carrigan, C. R. (2000). Plumbing Systems. In: Sigurdsson, H. (ed.) *Encyclopedia of Volcanoes*. Academic Press, 219–235.

Carrigan, C. R. & Eichelberger, J. C. (1990). Zoning of magmas by viscosity in volcanic conduits. *Nature* 343, 248–251.

Carrigan, C., Schubert, G. & Eichelberger, J. (1992). Thermal and dynamical regimes of single- and two-phase magmatic flow in dikes. *Journal of Geophysical Research* 97(B12): doi: 10.1029/92JB01244.

Castruccio, A., Rust, A. C. & Sparks, R. S. J. (2010). Rheology and flow of crystal-bearing lavas: Insights from analogue gravity currents. *Earth and Planetary Science Letters* 297, 471-480, doi:10.1016/ j.epsl.2010.06.051.

Charrier, A. D. & Marsh, B. D. (2004). Sill emplacement dynamics from regional flow sorting of opx phenocrysts, Basement Sill, McMurdo Dry Valleys, Antarctica. *Eos Trans. AGU* 85 (17), Jt. Assem. Suppl., Abstract V42A-03.

Costa, A. (2005). Viscosity of high crystal content melts: Dependence on solid fraction. *Geophysical Research Letters* 32, L22308: doi:10.1029/2005GL024303.

Couch, S., Sparks, R. S. J. & Carroll, M. R. (2001). Mineral disequilibrium in lavas explained by convective self-mixing in open magma chambers. *Nature* 411, 1037-1039.

Dawson, J. B. & Hawthorne, J. B. (1973). Magmatic sedimentation and carbonatitic differentiation in kimberlite sills at Benfontein, South Africa. *Journal of the Geological Society of London* 129 (1), 61-85.

Delaney, P. T. & Pollard, D. D. (1982). Solidification of basaltic magma during flow in a dike. *American Journal of Science* 282, 856-885.

Eichelberger, J. C. (1980). Vesiculation of mafic magma during replenishment of silicic magma reservoirs. *Nature* 288, 446-450.

Eichelberger, J. C., Chertkoff, D. G., Dreher, S. T. & Nye, C. J. (2000). Magmas in collision: Rethinking chemical zonation in silicic magmas. *Geology* 28 (7), 603-606.

Field, M., Gernon, T. M., Mock, A., Walters, A., Sparks, R. S. J. & Jerram, D. A. (2009). Variations of olivine abundance and grain size in the Snap Lake kimberlite intrusion, Northwest Territories, Canada: A possible proxy for diamonds. *Lithos* 112S, 23–35.

Green, D. H. & Ringwood, A. E. (1967). The genesis of basaltic magmas. *Contributions to Mineralogy and Petrology* 15 (2), 103-190.

Greenough, J. D., Ruffman, A. & Owen, J. V. (1988). Magma injection directions inferred from a fabric study of the Popes Harbour dike, eastern shore, Nova Scotia, Canada. *Geology* 16, 547-550.

Heaman, L. M., Kjarsgaard, B. A., Creaser, R. A. (2003). The timing of kimberlite magmatism in North America: implications for global kimberlite genesis and diamond exploration. *Lithos* 71, 153-184.

Heaman, L. M., Kjarsgaard, B. A, Creaser, R. A. (2004). The temporal evolution of North American kimberlites. *Lithos* 76, (1-4), 377-397.

Higgins, M. D. (2006). Quantitative textural measurements in igneous and metamorphic petrology. Cambridge University Press.

Holness, M. B. & Humphreys, M. C. S. (2003). The Traigh Bhàn na Sgùrra sill, Isle of Mull: Flow localization in a major magma conduit. *Journal of Petrology* 44 (11), 1961-1976.

Huppert, H. E. & Sparks, R. S. J. (1988). The generation of granitic magmas by intrusion of basalt into continental crust. *Journal of Petrology* 29 (3), 599-624.

Kelley, S. P. & Wartho, J. A. (2000). Rapid kimberlite ascent and the significance of Ar-Ar ages in xenolith phlogopites. *Science* 289, 609-611.

Komar, P. D. (1972a). Mechanical interactions of phenocrysts and flow differentiation of igneous dikes and sills. *Bulletin of the Geological Society of America* 83 (4), 973-988.

Komar, P. D. (1972b). Flow differentiation in igneous dikes and sills; profiles of velocity and phenocryst concentration. *Bulletin of the Geological Society of America* 83 (11), 3443-3448.

Komar, P. D. (1976). Phenocryst interactions and the velocity profile of magma flowing through dykes or sills. *Bulletin of the Geological Society of America* 87, 1336–1342.

Kopylova, M.G., Mogg, T. and Scott Smith, B. (2010). Mineralogy of the Snap Lake kimberlite, Northwest Territories, Canada, and compositions of phlogopite as records of its crystallisation. *The Canadian Mineralogist* 48, 549-570.

Koyaguchi, T. & Takada, A. (1994). An experimental study on the formation of composite intrusions from zoned magma chambers. *Journal of Volcanology and Geothermal Research* 59, 261–267.

Kurszlaukis, S. & Barnett, W. (2003). Volcanological and structural aspects of the Venetia kimberlite cluster – a case study of South African kimberlite maar-diatreme volcanoes. *South African Journal of Geology* 106, 145-172.

Marsh, B. D. (1981). On the crystallinity, probability of occurrence, and rheology of lava and magma. *Contributions to Mineralogy and Petrology* 78 (1), 85-98.

Marsh, B. D. (1996). Solidification Fronts and Magmatic Evolution. *Mineralogical Magazine* 60 (398), 5-40.

Martin, D. & Nokes, R. (1988). Crystal settling in a vigorously converting magma chamber. *Nature* 332, 534-536.

McBean, D., Kirkley, M. & Revering, C. (2003). Structural controls on the morphology of the Snap Lake kimberlite dyke. In: 8th International Kimberlite Conference, Extended Abstracts, 69-74.

McBirney, A. R. (1980). Mixing and unmixing of magmas. *Journal of Volcanology and Geothermal Research* 7 (3-4), 357-371.

Mitchell, R. H. (1986). Kimberlites: Mineralogy, Geochemistry, and Petrology. Plenum Press.

Mitchell, R. H. (2008). Petrology of hypabyssal kimberlites: Relevance to primary magma compositions. *Journal of Volcanology and Geothermal Research* 174, 1–8.

NIH (2006). ImageJ software package, U.S. National Institute of Health. URL http://rsb.info.nih.gov/ij/download.html.

Ogilvie-Harris, R., Sparks, R.S.J., Field, M. & Gernon, T.M. (2009). The Geochemistry of the

Snap Lake kimberlite dyke, NW Territories, Canada: Phlogopite and Spinel. Eos Trans. AGU, 90(22), Jt. Assem. Suppl., Abstract V33D-01.

Petford, N., Jerram, D. & Davidson, J. (2005). Slurry flow and structures formation in a magma mush: the Basement Sill, McMurdo Dry Valleys, Antarctica. *Eos Trans. AGU* 86 (52), Fall Meet. Suppl., Abstract V13H-05.

Philpotts, A. R. & Asher, P. M. (1993). Wallrock Melting and Reaction Effects along the Higganum Diabase Dike in Connecticut: Contamination of a Continental Flood Basalt Feeder. *Journal of Petrology* 34 (5), 1029-1058.

O'Keefe, M. D. & Cruden, A. R. (1999). AMS and fabric study of the Snap Lake NW-peninsula kimberlite dyke. Unpublished report prepared for Winspear Resources Ltd., 106 pp.

Philpotts, A. R. & Asher, P. M. (1994). Magmatic flow-direction indicators in a giant diabase feeder dike, Connecticut. *Geology* 22, 363-366.

Philpotts, A. R. & Carroll, M. (1996). Physical properties of partly melted tholeiitic basalt. *Geology* 24 (11), 1029–1032.

Pinkerton, H. & Stevenson, R. J. (1992). Methods of determining the rheological properties of magmas at sub-liquidus temperatures. *Journal of Volcanology and Geothermal Research* 53(1-4), 47-66.

Preston, R. J. & Bell, B. R. (1997). Cognate gabbroic xenoliths from a tholeiitic subvolcanic sill complex; implications for fractional crystallization and crustal contamination processes. *Mineralogical Magazine* 61 (3), 329-349.

Price, S. E., Russell, J. K. & Kopylova, M. G. (2000). Primitive magma from the Jericho Pipe, N.W.T., Canada: Constraints on primary kimberlite melt chemistry. *Journal of Petrology* 41 (6), 789-808.

R (2006). The R Project for Statistical Computing. CRAN. URL: http://cran.r-project.org/

Richardson, J. F. (1971). Incipient fluidisation and particle systems. In: Davidson, J. F. & Harrison, D. (eds.) *Fluidisation*, Academic Press, London and New York, 26-64.

Roscoe, R. (1952). The viscosity of suspensions of rigid spheres. *British Journal of Applied Phys*ics 3, 267: doi: 10.1088/0508-3443/3/8/306.

Ross, M. E. (1986). Flow differentiation, phenocryst alignment and compositional trends within a dolerite dyke at Rockport, Massachusetts. *Bulletin of the Geological Society of America* 97, 232-240.

Shaw, H. R. (1965). Comments on viscosity, crystal settling, and convection in granitic magmas. *American Journal of Science* 263, 120-152.

Shelley, D. (1985). Determining paleo-flow directions from groundmass fabrics in the Lyttelton radial dykes, New Zealand. *Journal of Volcanology and Geothermal Research* 25, 69–79.

Smith, J. V. (2000). Textural evidence for dilatant (shear thickening) rheology of magma at high crystal concentrations. *Journal of Volcanology and Geothermal Research* 99, 1–7.

Sparks, R. S. J., Sigurdsson, H. & Wilson, L. (1977). Magma mixing: a mechanism for triggering acid explosive eruptions. *Nature* 267, 315-318.

Sparks, R. S. J., Huppert, H. E., Turner, J. S., Sakuyama M. & O'Hara, M. J. (1984). The Fluid Dynamics of Evolving Magma Chambers [and Discussion]. *Philosophical Transactions of the Royal Society of London* 310 (1514), 511-534.

Sparks, R. S. J., Baker, L., Brown, R. J., Field, M., Schumacher, J. Stripp, G. & Walters, A. (2006). Dynamical constraints on kimberlite volcanism. *Journal of Volcanology and Geothermal Research* 155 (1-2), 18-48.

Sparks, R. S. J., Brooker, R. A., Field, M., Kavanagh, J., Schumacher, J. C., Walter, M. J., White, J. (2009). The nature of erupting kimberlite melts. *Lithos* 1125, 429-438.

Spera, F. J. (2000). Physical Properties of Magma. In: Sigurdsson, H. (ed.) *Encyclopedia of Volcanoes*. Academic Press, New York, pp. 171-190.

Stubley, M. (2000). Bedrock geology of the Snap Lake area, Camsell Lake Property: A report to accompany a 1:10,000 scale geological map. Unpublished report, prepared for Winspear Resources Ltd.

Ventura, G., De Rosa, R., Colletta, E. & Mazzuoli, R. (1996). Deformation patterns in a high-viscosity Iava flow inferred from the crystal preferred orientation and imbrication structures: an example from Salina (Aeolian Islands, southern Tyrrhenian Sea, Italy). *Bulletin of Volcanology* 57, 555-562.

Wada, Y. (1992). Magma flow directions inferred from preferred orientations of phenocrysts in a composite feeder dyke, Miyake-Jima, Japan. *Journal of Volcanology and Geothermal Research* 49, 119-126.

FIGURE CAPTIONS

Figure 1: (a) Map of Canada showing the location of the Slave craton, Northwest Territories. (b) Summary geological maps of the Slave craton and (c) the Snap Lake area (modified after Stubley, 2000, unpublished data), showing the location of mine-works covered in this study; (d) NE-SW trending profile (see (c)) of the Snap Lake intrusion produced from vertical intercepts of kimberlite in boreholes. (e) Outline map of the Snap Lake Mine showing the locations of zones 1 and 2 (separated by vertical dashed line), and the generalised structural geology of the area (refer to (c) for location, and (d) for elevation data). Also included are the locations of sampling traverses ND1-01 and ND2-06 (inset), depicted in Figs. 4 & S1 respectively.

Figure 2: (a) Olivine-rich macrocrystic kimberlite (ORK), in which a strong sub-vertical fabric is discernible. (b) Rose plot shows the fabric defined by long-axis orientations of olivine crystals in the plane of the exposure shown in (a). The rose diagrams were extracted from photographs of sub-vertical faces, and rose diagrams are oriented with 90° indicating a vertical crystal orientation. Measurement interval = 10°. In rose diagrams, shading represents olivine long-axis length in mm (black: 5-10, dark grey: 10-20 and light grey: 20-50); the dashed line represents the % (labelled) of the total number of particles (N = 100). (c) SEM (backscattered-electron) photomicrograph of ORK sampled from the intrusion level shown in Fig. 2a (above); note the sub-vertical fabric defined by elongate serpentinised olivine (SO) crystals, in a fine-grained matrix comprising olivine microcrysts (see d), apatite (A), phlogopite (largely replaced by chlorite) and void-filling serpentine.

Figure 3: Summary map of the studied area showing six schematic graphic logs through typical sections of the intrusion. Rose diagrams show the fabric defined by long-axis orientations of olivine crystals in the plane of the exposure. The rose diagrams were extracted from photographs of sub-vertical faces, and rose diagrams are oriented with 90° indicating a vertical crystal orientation. Each plot relates to the corresponding level in the intrusion. Measurement interval = 10°. In rose diagrams, the dashed lines represents the % (labelled) of the total number of particles (N = 100 for each plot).

Figure 4: Schematic graphic log through the intrusion at locality ND1-01 in zone 1 (for location, see Fig. 1e). Images of exposures and SEM photomicrographs correspond to specific levels in the intrusion, labelled a-f. See caption to Fig. 2 for an explanation of the rose diagrams. Note that the top of the intrusion (a) is olivine-poor and contains high proportions of phlogopite laths, whereas the bulk of the intrusion (b)-(f) is characteristically olivine-rich, with lesser proportions of phlogopite; D = dolomite and C = chlorite, after phlogopite.

Figure 5: (a)-(b) Photographs of olivine-poor, phlogopite-rich kimberlite (OPK) from the intrusion; note the patchy appearance, particularly in (b). (c)-(d) SEM (backscattered-electron) image of altered macrocrysts (serpentinised olivine), phlogopite laths (enclosing probable monticellite) and void-filling serpentine. (e) SEM image of a marginal, heavily veined region of the intrusion, containing antigorite (replacing olivine), altered phlogopite and void-filling serpentine and dolomite.

Figure 6: Graphs showing the relationship between intrusion thickness and: (a) maximum olivine size, and (b) olivine crystal content. Dashed lines are shown to summarise the main trends; horizontal dashed lines depict an abrupt change in crystal size and content above a specific

intrusion thickness.

Figure 7: Map summarising the spatial distribution of ramps across a test panel in zone 2 of the mine (for location refer to Fig. 1e). Also shown are the variations in (b) maximum crystal size (symbol as in Fig. S2), (c) mean crystal size (depicted as scaled light grey circles, see legend), and (d) olivine crystal content (symbol as in Fig. 8).

Figure 8: Schematic cross-section of the internal structure of the intrusion in zone 2 (see inset for location). Rose diagrams show the fabric defined by long-axis orientations of olivine crystals in the plane of the exposure. Note the dominantly sub-vertical alignment of olivine crystals. Measurement interval = 10°. In rose diagrams, the dashed line represents 10% of the total number of crystals (N = 100).

Figure 9: (a) Olivine-rich lithic breccia (OR_{Br}) containing concentrations of olivine crystals in the interstices between lithic clasts. Note the sharp contact with OPK. (b) Olivine-poor lithic breccia (OP_{Br}) occurring in a wedge-shaped irregularity in the hangingwall of the intrusion associated with a ramp system. (c) Distribution of lithic clasts in a typical ramp from zone 1 in the SLI (Fig. 1e). (d) Graph showing the variation in lithic proportion with distance from the ramp depicted in (c).

Figure 10: Schematic cross-section illustrating the three key stages involved in ramp formation in the SLI and breccia emplacement. See text for further details.

Figure 11: (a) Schematic summary of structural complexities and lithofacies relationships within the SLI. Heterogeneities in crystal size and content occur over short distances (metres to tens of metres) in the intrusion. Inset: entrainment of cognate xenolith of ORK by relatively mobile OPK

magma. (b) Schematic cartoons of fabric generation in the intrusion. When late-stage ORK magma is injected in the centre of the intrusion, the parallel “plates” pull apart to accommodate flowing magma. Consequently, elongate olivine crystals are rotated into more stable sub-vertical orientations.

Figure 12: (a) Ratio of groundmass viscosity (μ_g) to melt viscosity (μ_{melt}) as a function of crystal content (ϕ) showing the asymptotic increase in melt viscosity due to the addition of crystals. μ_g is calculated using a modified Einstein-Roscoe equation (equation 1) presented in Castruccio et al. (2010). (b) Timescale of crystal settling (t_s) as a function of depth (z) over a range of melt viscosities (values given are in Pa s), where $\phi = 0$. Crystal settling times were calculated using the appropriate equations 4 and 5, depending on the value of Re_p (equation 2). For b & c, the crystal diameter (d_p) = 0.01 m, and $\Delta\rho = 500$ kg m^{-3}. (c) Timescale of crystal settling (t_s) as a function of depth for $\mu = 0.1$ Pa s at different crystal concentrations, $\phi = 0$, $\phi = 0.4$ and $\phi = 0.6$ (grey shaded area). The curves were calculated using the equation (6) for hindered settling (Richardson, 1971) and equation 5. Also shown for comparison is the timescale for conductive cooling (t_c) of a 4 m thick intrusion, assuming a thermal diffusivity of 8×10^{-7} m^2 s^{-1}.

SUPPLEMENTARY DATA

Figure S1: Schematic graphic log through the intrusion at locality ND2-06 in zone 2 (for location, see the inset map and Fig. 1e). Images of exposures and SEM photomicrographs correspond to specific levels in the intrusion, labelled (a)-(f). The intrusion can broadly be divided into three units: (1) olivine-poor and phlogopite rich (a & g); (2) olivine-rich and phlogopite-poor (c & d), and (3) olivine and phlogopite-rich (e & f). See caption to Fig. 4 for an explanation of the rose diagrams.

Figure S2: Series of maps of zone 1 of the intrusion (see Figs. 1c & 1e) summarising (a) the variations in maximum crystal size (scaled black circles, see legend) and intrusion thickness (vertical lines), and (b) the variations in crystal content (depicted as pie charts, see legend) and intrusion thickness.

Figure S3: Summary map of part of zone 2 of the SLI (Fig. 1e) depicting 19 schematic graphic logs through the intrusion; note the significant variations in lithofacies geometry and distribution over metre to tens of metre scales.

Figure S4: Schematic cross-section of the internal structure of the intrusion in part of zone 2 (Fig. 1e; see inset for traverse location). Refer to the caption of Fig. 10 for an explanation of the rose diagrams.

Figure S5: Schematic cross-section of the internal structure of the intrusion in part of zone 2 (Fig. 1e; see inset for traverse location). Refer to the caption of Fig. 10 for an explanation of the rose diagrams.

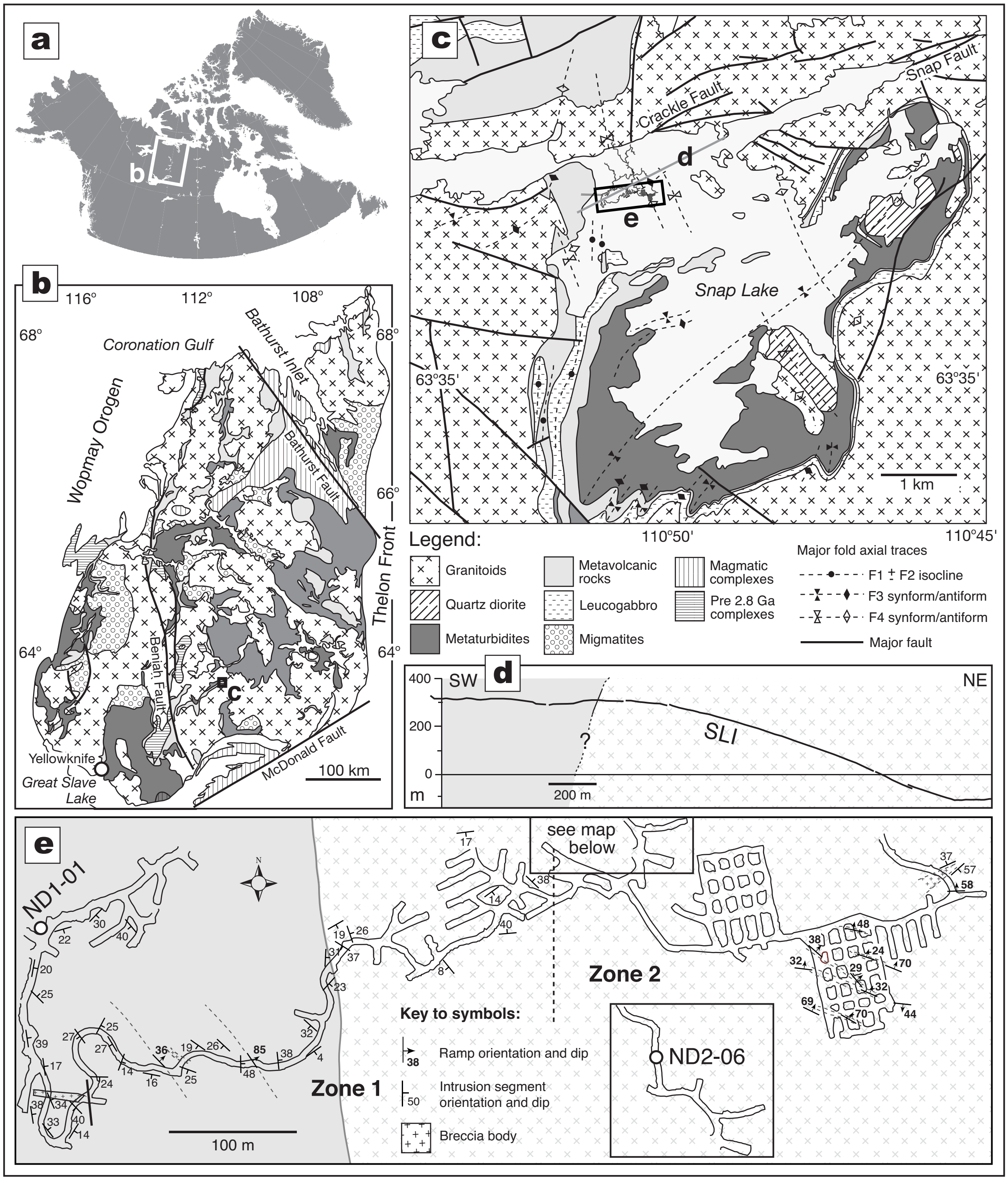
a
b
c
d
e
116°
112°
108°
68°
66°
64°
Coronation Gulf
Bathurst Inlet
Bathurst Fault
Wopmay Orogen
Thelon Front
Beniah Fault
McDonald Fault
Yellowknife
Great Slave Lake
100 km
Snap Fault
Crackle Fault
Snap Lake
63°35'
110°50'
110°45'
1 km
Legend:
Granitoids
Quartz diorite
Metaturbidites
Metavolcanic rocks
Leucogabbro
Migmatites
Magmatic complexes
Pre 2.8 Ga complexes
Major fold axial traces
F1 ± F2 isocline
F3 synform/antiform
F4 synform/antiform
Major fault
SW
NE
400
200
0
m
?
SLI
200 m
see map below
ND1-01
N
Zone 1
Zone 2
ND2-06
Key to symbols:
Ramp orientation and dip
Intrusion segment orientation and dip
Breccia body
100 m

Figure 1

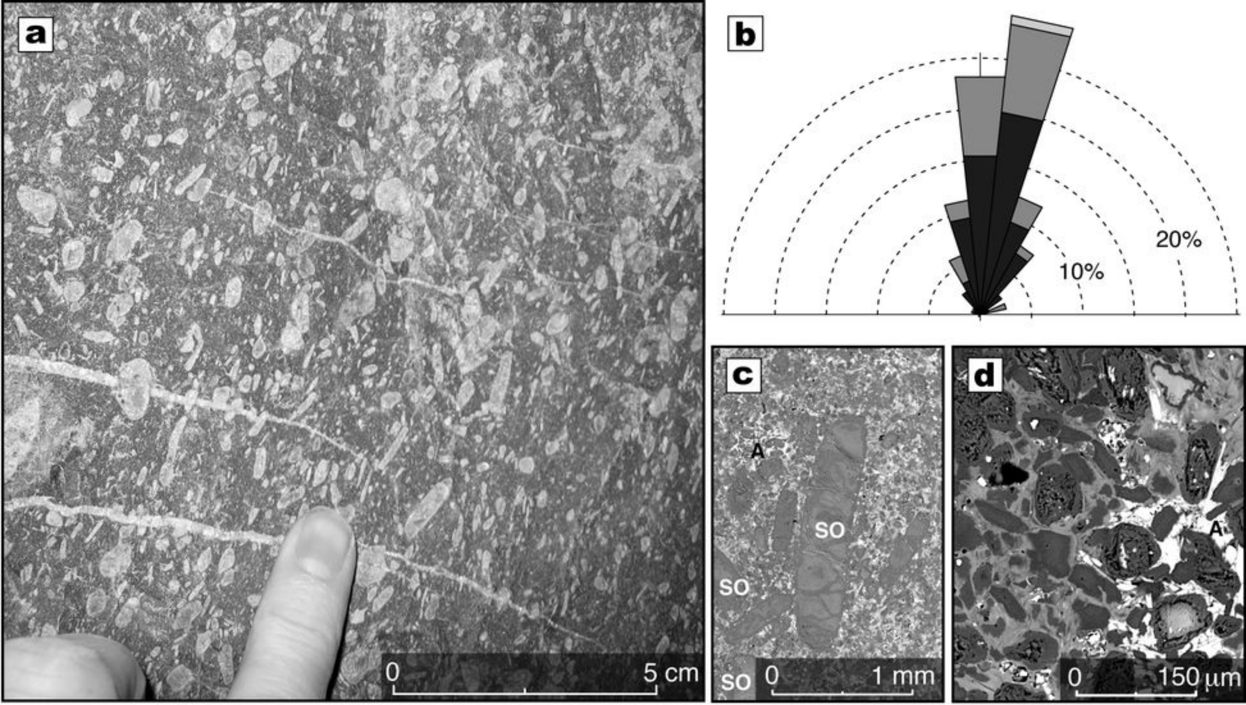

Figure 2

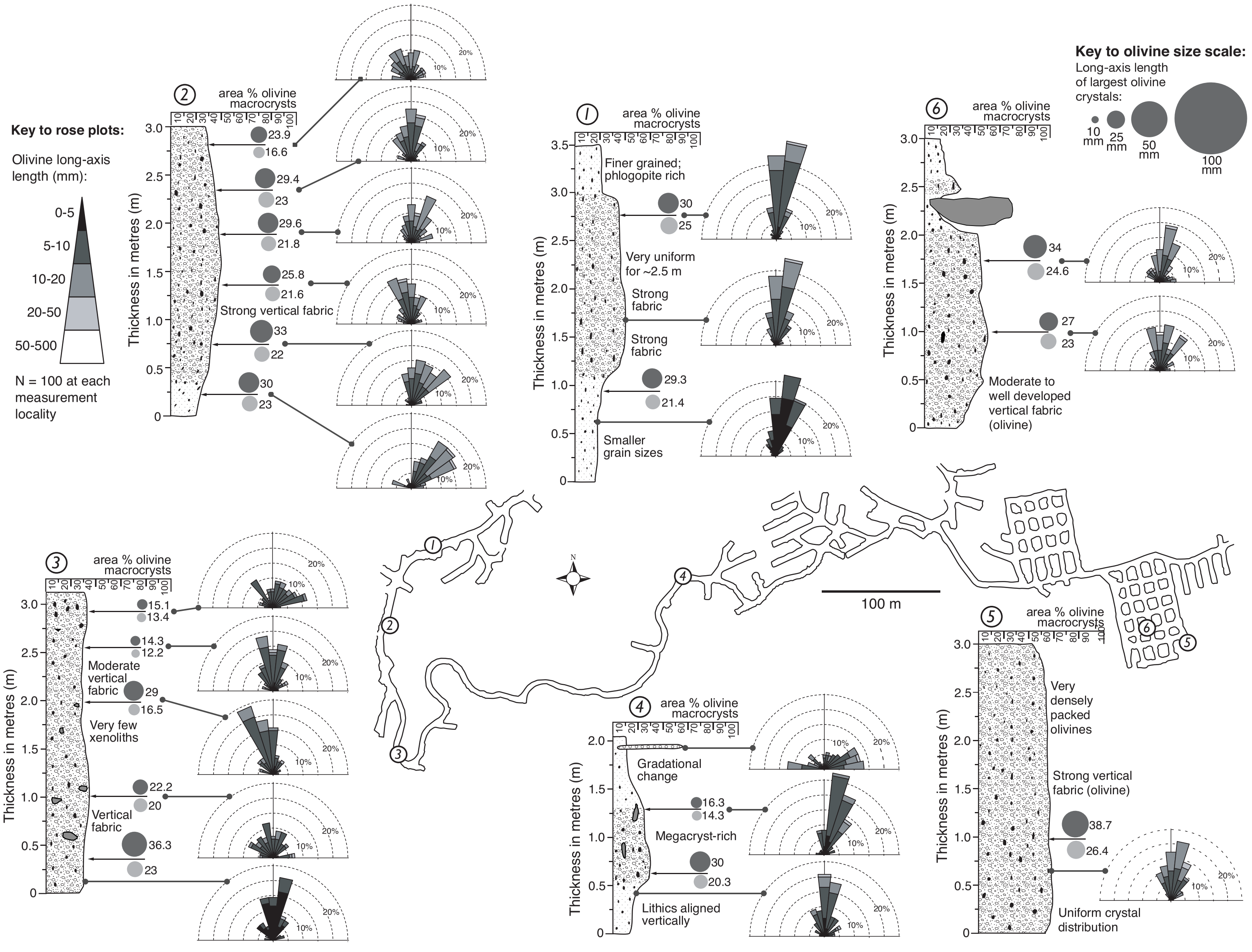
Key to rose plots:
Olivine long-axis length (mm):
0-5
5-10
10-20
20-50
50-500
N = 100 at each measurement locality
Key to olivine size scale:
Long-axis length of largest olivine crystals:
10 mm
25 mm
50 mm
100 mm
②
area % olivine macrocrysts
Thickness in metres (m)
23.9
16.6
29.4
23
29.6
21.8
25.8
21.6
Strong vertical fabric
33
22
30
23
①
Finer grained; phlogopite rich
30
25
Very uniform for ~2.5 m
Strong fabric
Strong fabric
29.3
21.4
Smaller grain sizes
⑥
34
24.6
27
23
Moderate to well developed vertical fabric (olivine)
③
15.1
13.4
14.3
12.2
Moderate vertical fabric
29
16.5
Very few xenoliths
22.2
20
Vertical fabric
36.3
23
④
Gradational change
16.3
14.3
Megacryst-rich
30
20.3
Lithics aligned vertically
⑤
Very densely packed olivines
Strong vertical fabric (olivine)
38.7
26.4
Uniform crystal distribution
N
100 m
10%
20%

Figure 3

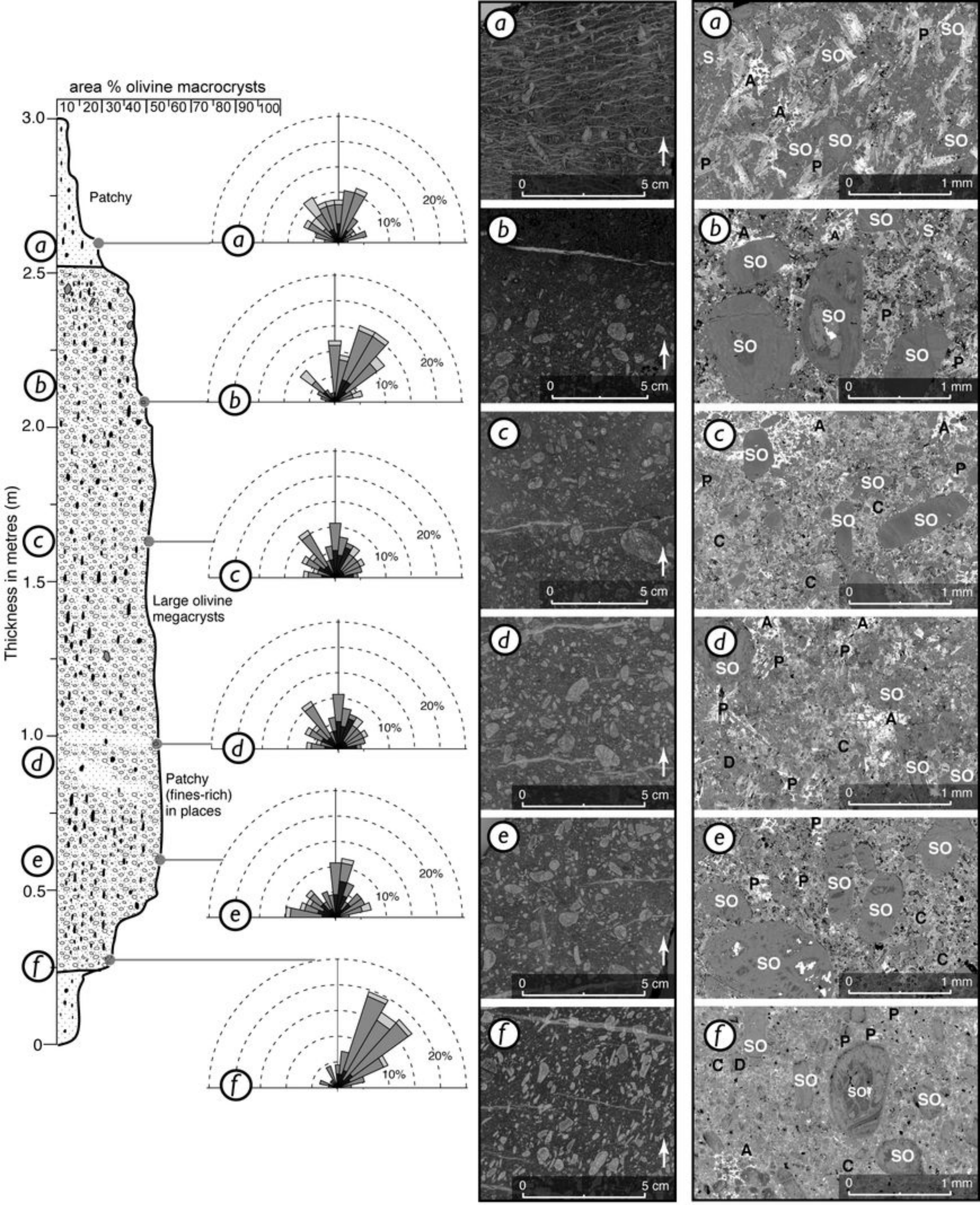
area % olivine macrocrysts
10 20 30 40 50 60 70 80 90 100
Thickness in metres (m)
3.0
2.5
2.0
1.5
1.0
0.5
0
Patchy
Large olivine megacrysts
Patchy (fines-rich) in places
a
b
c
d
e
f
20%
10%
5 cm
0
1 mm
SO
A
P
S
C
D

Figure 4

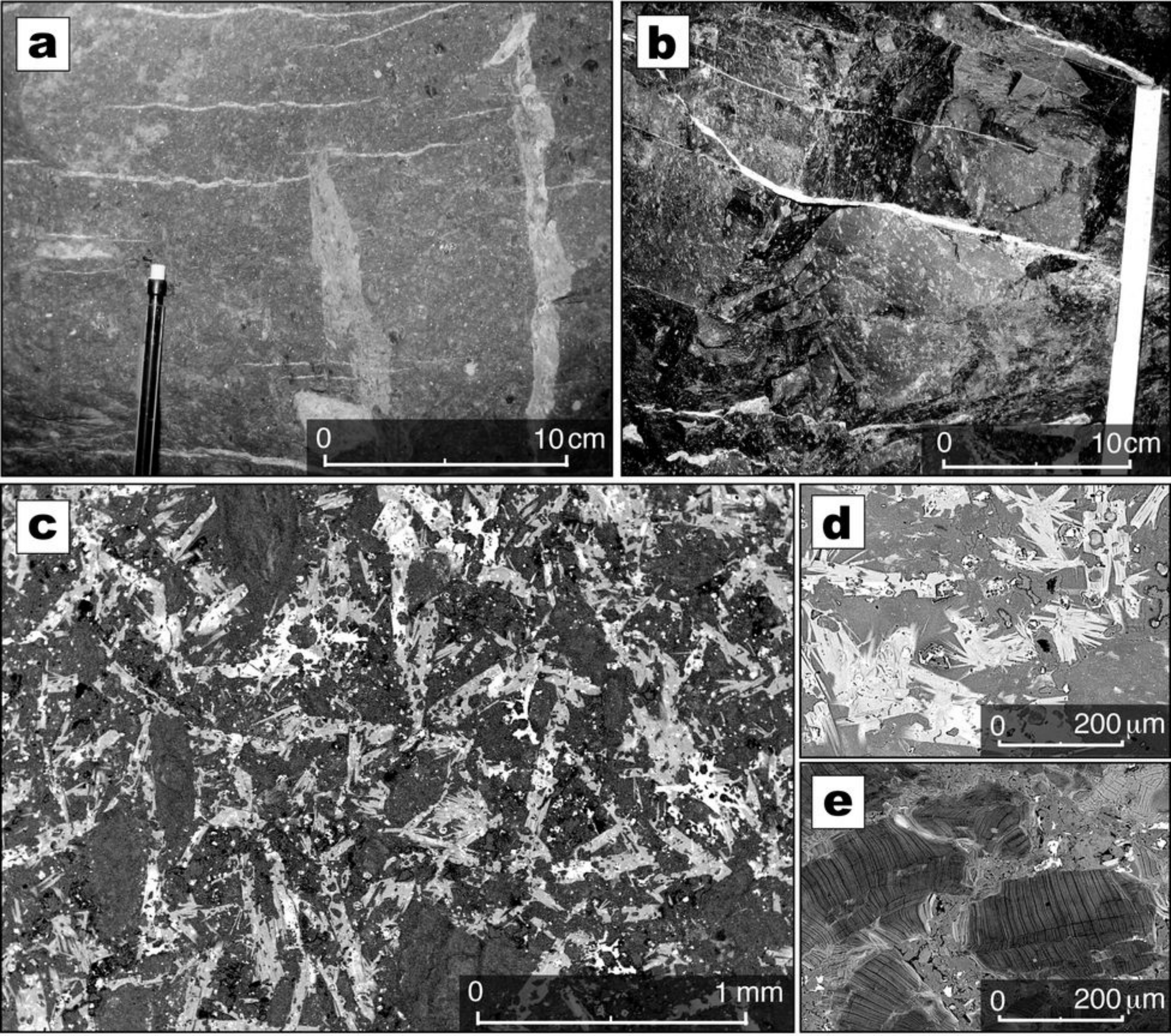

Figure 5

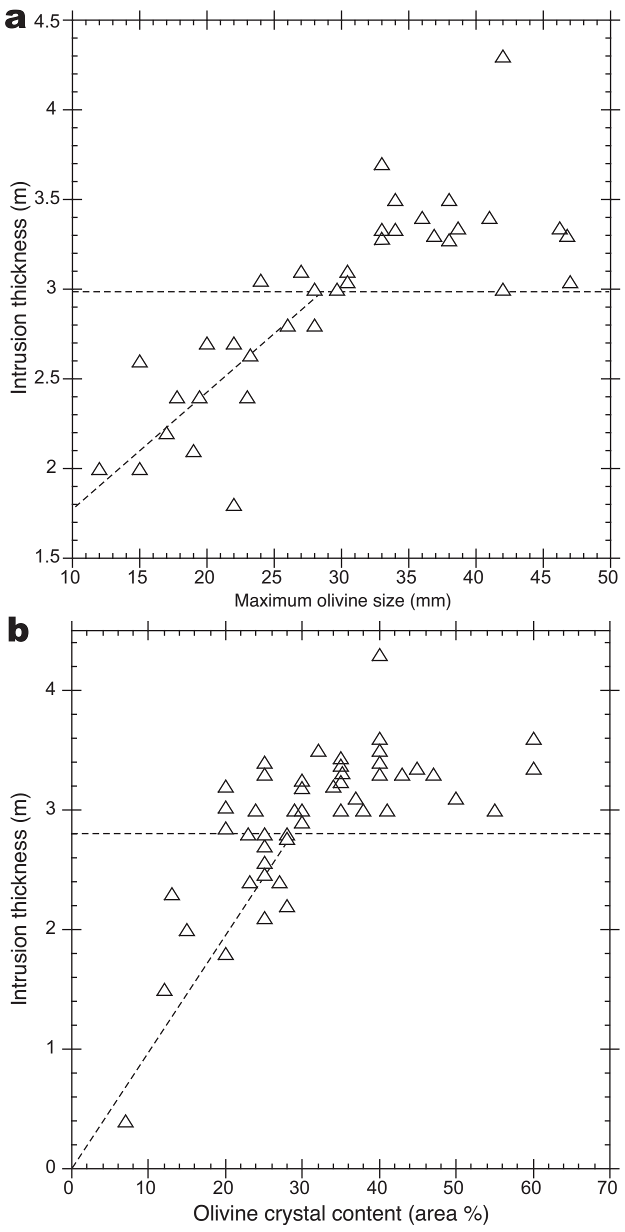
a
Intrusion thickness (m)
1.5
2
2.5
3
3.5
4
4.5
Maximum olivine size (mm)
10
15
20
25
30
35
40
45
50
b
Intrusion thickness (m)
0
1
2
3
4
Olivine crystal content (area %)
0
10
20
30
40
50
60
70

Figure 6

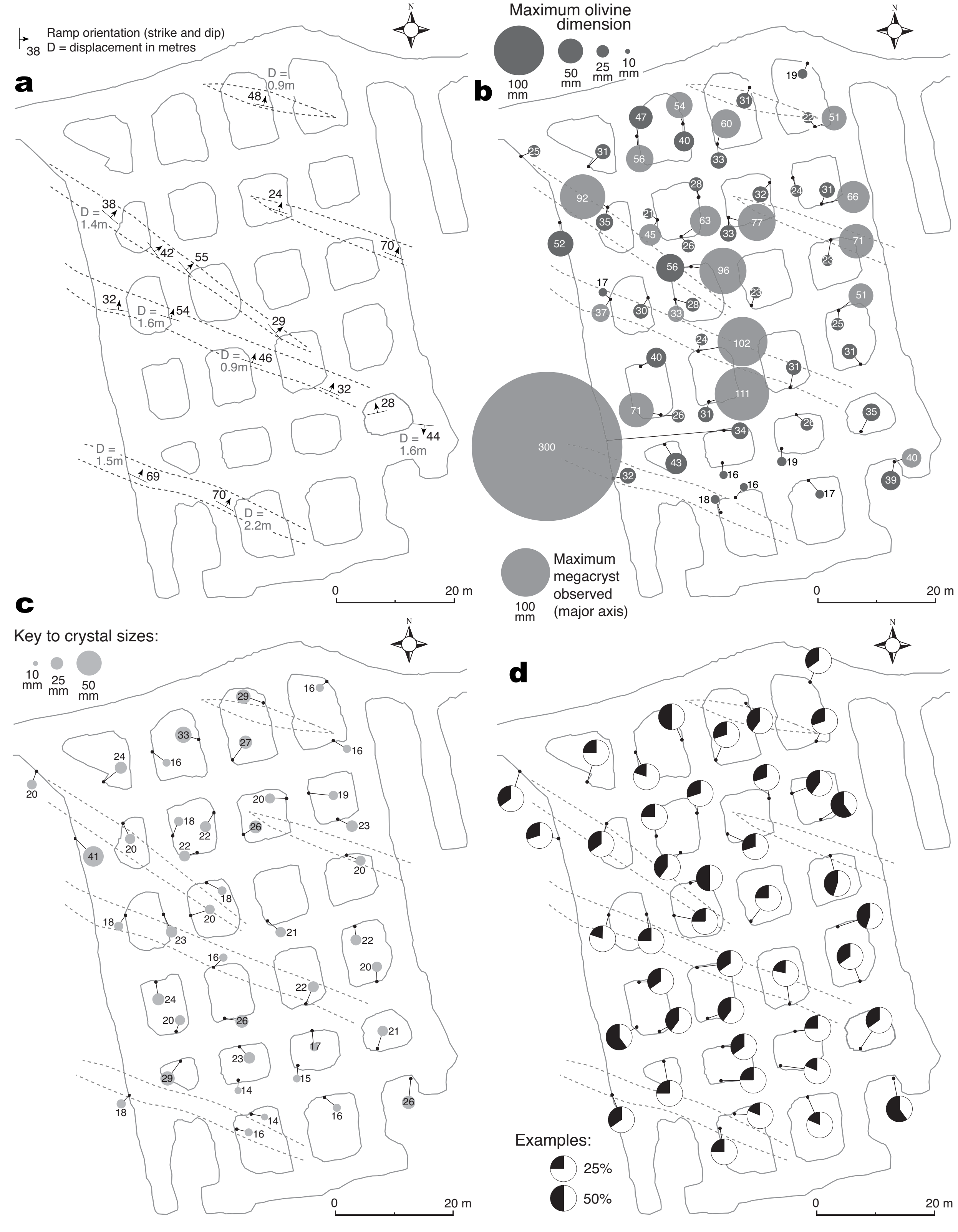

38 Ramp orientation (strike and dip)
D = displacement in metres
a
D = 0.9m
48
24
38
D = 1.4m
42
55
70
32
D = 1.6m
54
29
D = 0.9m
46
32
28
D = 1.6m
44
D = 1.5m
69
70
D = 2.2m
0
20 m
N
Maximum olivine dimension
100 mm
50 mm
25 mm
10 mm
b
19
31
54
47
60
22
51
40
31
56
33
25
28
32
24
31
66
92
63
77
21
45
35
26
33
52
71
23
56
96
17
23
51
37
30
33
28
25
24
102
40
31
31
71
26
111
31
35
34
26
300
43
19
40
16
32
39
16
17
18
Maximum megacryst observed (major axis)
100 mm
c
Key to crystal sizes:
10 mm
25 mm
50 mm
29
16
33
27
24
16
16
20
20
19
18
26
22
23
41
20
22
20
18
20
18
23
21
22
16
20
22
24
20
26
21
23
17
29
14
15
18
14
16
16
26
d
Examples:
25%
50%

Figure 7

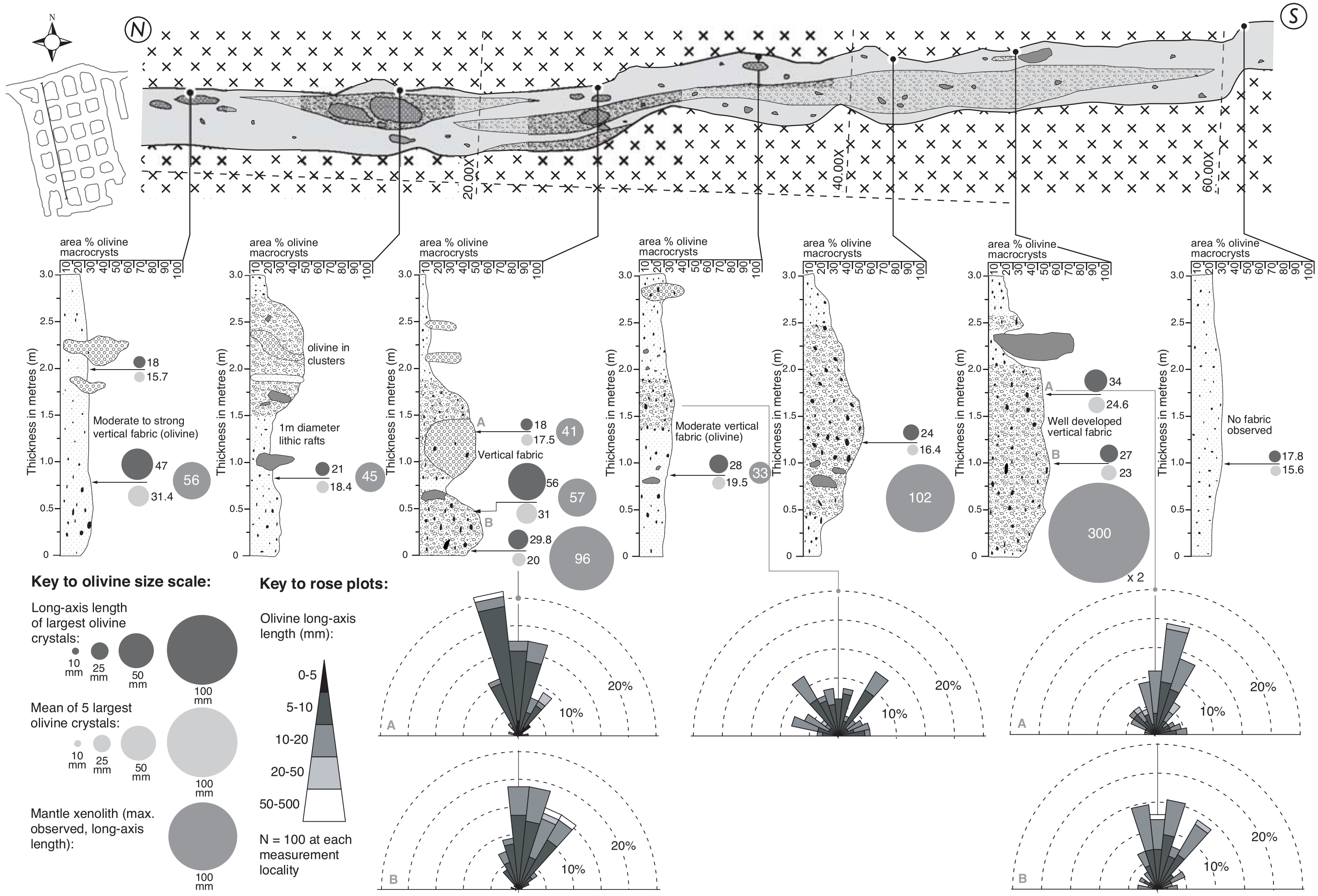
N
S
20.00X
40.00X
60.00X
area % olivine macrocrysts
10 20 30 40 50 60 70 80 90 100
Thickness in metres (m)
3.0
2.5
2.0
1.5
1.0
0.5
0
18
15.7
Moderate to strong vertical fabric (olivine)
47
31.4
56
olivine in clusters
1m diameter lithic rafts
21
18.4
45
A
18
17.5
41
Vertical fabric
56
57
B
31
29.8
20
96
Moderate vertical fabric (olivine)
28
19.5
33
24
16.4
102
A
34
24.6
Well developed vertical fabric
B
27
23
300
x 2
No fabric observed
17.8
15.6
Key to olivine size scale:
Long-axis length of largest olivine crystals:
10 mm
25 mm
50 mm
100 mm
Mean of 5 largest olivine crystals:
10 mm
25 mm
50 mm
100 mm
Mantle xenolith (max. observed, long-axis length):
100 mm
Key to rose plots:
Olivine long-axis length (mm):
0-5
5-10
10-20
20-50
50-500
N = 100 at each measurement locality
10%
20%
A
B

Figure 8

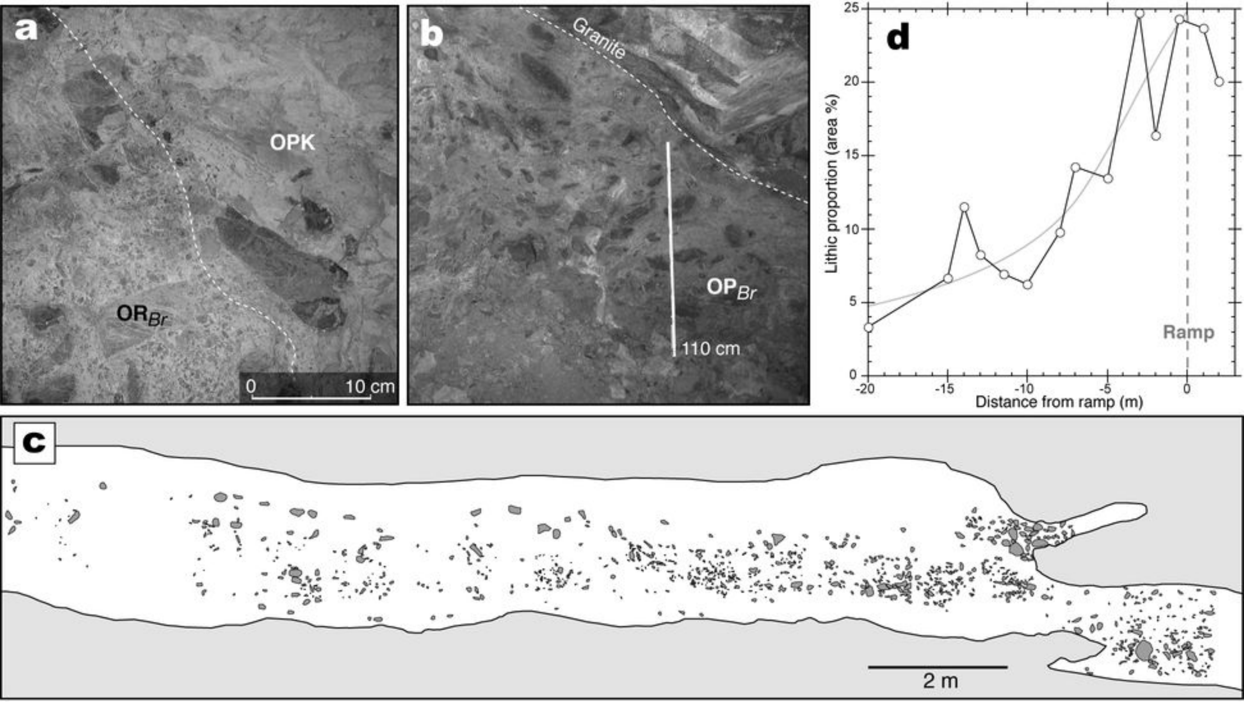
a
OPK
OR$_{Br}$
0
10 cm
b
Granite
OP$_{Br}$
110 cm
d
Lithic proportion (area %)
0
5
10
15
20
25
-20
-15
-10
-5
0
Distance from ramp (m)
Ramp
c
2 m

Figure 9

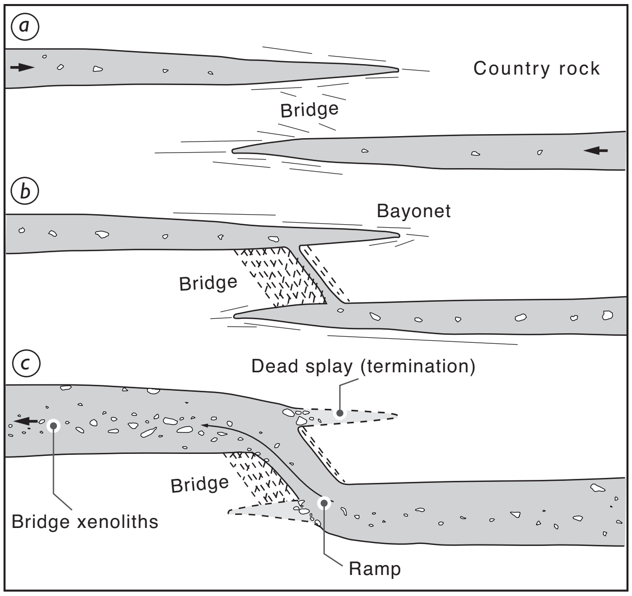
a
Country rock
Bridge
b
Bayonet
Bridge
c
Dead splay (termination)
Bridge
Bridge xenoliths
Ramp

Figure 10

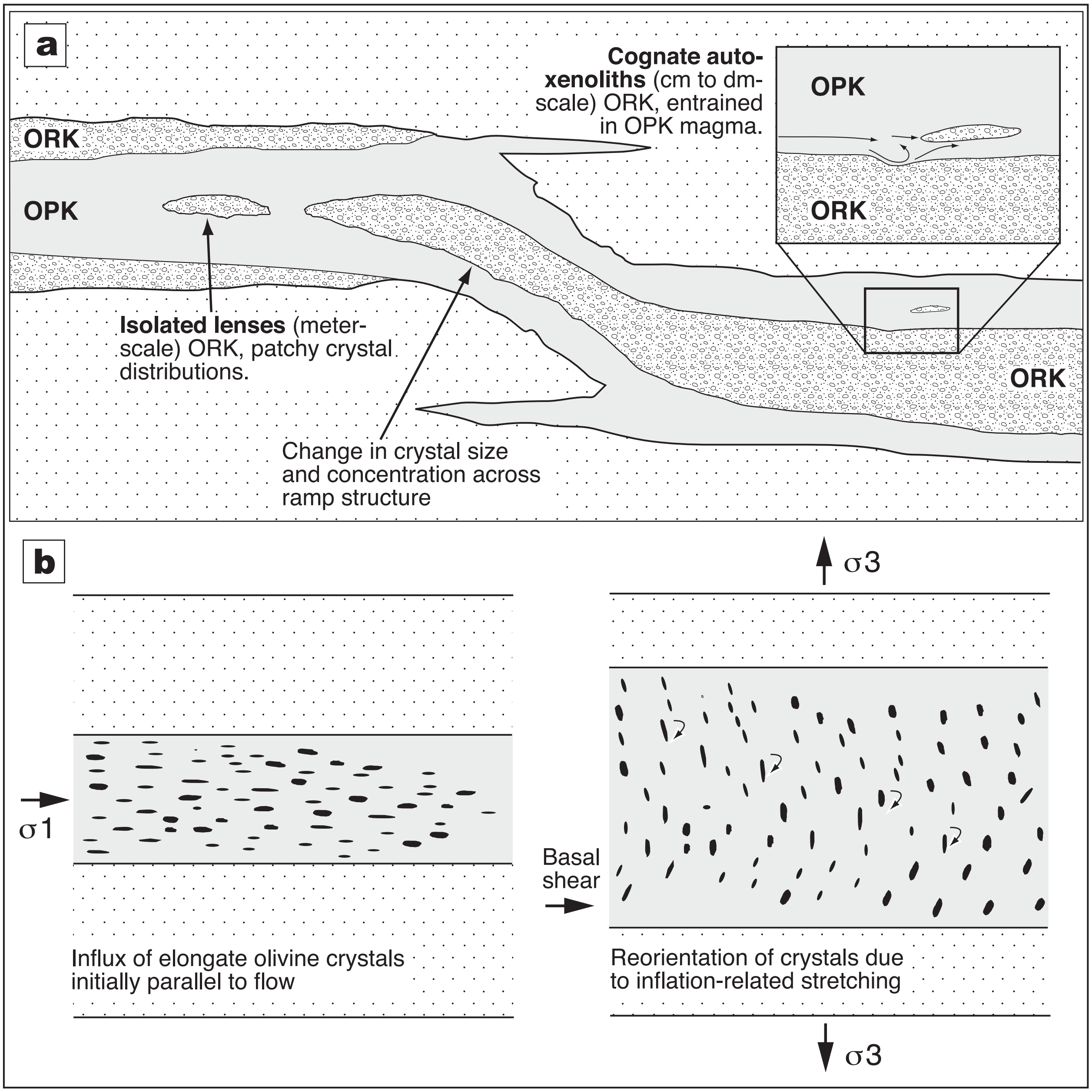
a
Cognate auto-xenoliths (cm to dm-scale) ORK, entrained in OPK magma.
OPK
ORK
ORK
OPK
Isolated lenses (meter-scale) ORK, patchy crystal distributions.
Change in crystal size and concentration across ramp structure
ORK
b
σ1
Influx of elongate olivine crystals initially parallel to flow
Basal shear
σ3
Reorientation of crystals due to inflation-related stretching
σ3

Figure 11

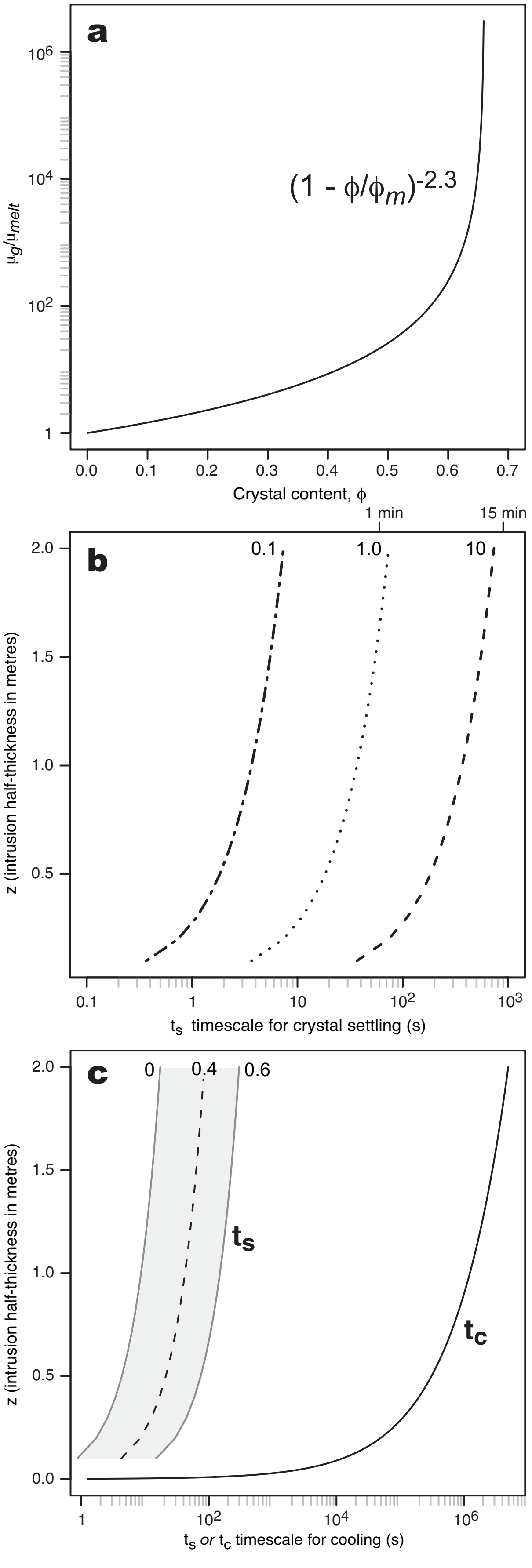
a
(1 - ϕ/ϕ_m)^-2.3
μg/μmelt
1
10^2
10^4
10^6
0.0
0.1
0.2
0.3
0.4
0.5
0.6
0.7
Crystal content, ϕ
b
1 min
15 min
0.1
1.0
10
z (intrusion half-thickness in metres)
0.5
1.0
1.5
2.0
0.1
1
10
10^2
10^3
ts timescale for crystal settling (s)
c
0
0.4
0.6
ts
tc
z (intrusion half-thickness in metres)
0.0
0.5
1.0
1.5
2.0
1
10^2
10^4
10^6
ts or tc timescale for cooling (s)